Spectral analysis of three-dimensional photonic jets

A. Devilez, B. Stout, N. Bonod, E. Popov

Spectral analysis of three-dimensional photonic jets

Alexis Devilez, Brian Stout, Nicolas Bonod, Evgeny Popov

Institut Fresnel, Aix-Marseille Université, CNRS
Domaine Universitaire de St Jérôme, 13397 Marseille, France
alexis.devilez@fresnel.fr

Abstract: The spatial and spectral properties of three-dimensional photonic jets are studied in a framework employing rigorous Lorentz-Mie theory. The contributions to the field from each spectral component are studied quantitatively and highlight the distinctive features of photonic jets. In particular, the presence of secondary lobes in the propagative frequency distribution are singled out as a fundamental distinctive property between photonic jets and classical Gaussian beams. It is shown that these differences can lead to divergences of photonic jets at least twice as small as those in corresponding 'Gaussian' beams.

OCIS codes: (230.3990) Micro-optical devices; (290.4020) Mie theory; (260.2110) Electromagnetic optics; (290.5850) Scattering, particles;

References and Links

1. Z. Chen, A. Taflove, V. Backman, "Photonic nanojet enhancement of backscattering of light by nanoparticles: a potential novel visible-light ultramicroscopy technique," Opt. Express **12**, 1214 - 1220 (2004).
2. X. Li, Z. Chen, A. Taflove, V. Backman, "Optical analysis of nanoparticles via enhanced backscattering facilitated by 3-D photonic nanojets," Opt. Express **13**, 526 - 533 (2005).
3. Z. Chen, A. Taflove, X. Li, V. Backman, "Superenhanced backscattering of light by nanoparticles," Opt. Letters **31**, 196 - 198 (2006).
4. A. Heifetz, K. Huang, A. V. Sahkian, X. li, A. Taflove, V. Backman, "Experimental confirmation of backscattering enhancement induced by a photonic jet," Appl. Phys. Lett. **89**, 221118 (2006).
5. P. Ferrand, J. Wenger, M. Pianta, H. Rigneau, A. Devilez, B. Stout, N. Bonod, E. Popov, "Direct imaging of photonic nanojet," Opt. Express (to be published).
6. D. Grojo, P. Delaporte, A. Cros, "Removal of particles by impulsional laser," Journal de Physique **IV 127**, 145 - 149 (2005).
7. S. M. Huang, M. H. Hong, B. Luk'yanchuk, T. C. Chong, "Nanostructures fabricated on metal surfaces assisted by laser with optical near-field effects," Appl. Phys. A: Mater. Sci. Process. **77**, 293 - 296 (2003).
8. W. Guo, Z. B. Wuang, L. Li, D. J. Whitehead, B. S. Luk'yanchuk, Z. Liu, "Near-field laser parallel nanofabrication of arbitrary-shaped patterns," Appl. Phys. Lett. **90**, 243101 (2007).
9. S.Lecler, S. Haacke, N. Lecong, O. Crégut, J. L. Rehspringer, C. Hirlimann, "Photonic jet driven non-linear optics: example of two-photon fluorescence enhancement by dielectric microspheres," Opt. Express **15**, 4935 - 4942 (2007).
10. S. Lecler, Y. Takakura, P. Meyrueis, "Properties of a three-dimensional photonic jet," Opt. Letters **30**, 2641 - 2643 (2005).
11. A. V. Itagi, W. A. Challener, "Optics of photonic nanojets," J. Opt. Soc. Am A **22**, 2847 - 2858 (2005).
12. B. Stout, M. Nevière, E. Popov, "Light diffraction by three-dimensional object: differential theory," J. Opt. Soc. Am. A **22**, 2385 - 2404 (2005).
13. O. Moine, B. Stout, "Optical force calculations in arbitrary beams by use of the vector addition theorem," J. Opt. Soc. Am. B **22**, 1620 - 1631 (2005).
14. W. J. Wiscombe, "Improved Mie scattering algorithms," Appl. Opt. **19**, 1505 - 1509 (1980).
15. M. Born and E. Wolf, "Elements of the theory of diffraction," in *Principles of Optics*, M. Born and E. Wolf (Pergamon press, 1986), pp. 370 - 458.

1. Introduction

Scattering of light by microspheres is an old and well known problem, analytically solved a century ago by Mie. This classical problem has recently received renewed interest by Chen et al. who reported the existence of 'photonic jets' in FDTD calculations [1-3]. Their simulations showed that when illuminating cylinders [1] or spheres [2] with plane waves, one can produce narrow beams in the near field of the shadow-side surface. These beams typically have FWHM (Full Width at Half Maximum) waists smaller than the incident wavelength and remain subwavelength over distances of several wavelengths. Moreover, the intensity can be hundreds of times higher than the incident intensity [2]. The existence of photonic jets has since been experimentally confirmed in microwaves range [4], and directly observed in the optical waves range with a confocal microscope operating in detection mode [5].

The ability of microspheres to focus light and enhance the electromagnetic (EM) field was previously known and utilized to remove particles from a substrate in laser dry cleaning technique [6]. Arrays of particles-lenses were proposed in 2003 as a technique to pattern a substrate with neither mask nor lithographic processes [7]. This technique enables one to pattern various shapes by illuminating the array at different angles [8]. The subwavelength properties of photonic jets and the advent of nanosciences and biotechnology, recommend photonic jets as a useful tool in high resolution tool for nano-particles detection [1-3], fluorescence microscopy improvements [9] and nanopatterning [7,8]. A fuller understanding of this beam is nevertheless needed to fully exploit the potential of microspheres as optical components.

Until now, photonic jets have principally been described in analogy with geometric optics focusing, considering the maximal enhancement of the spot as the focal point [10]. Although this analogy with focusing by spherical lenses does indeed yield certain insights, it does not explain the most interesting photonic jets properties, *i.e.* subwavelength waists and low divergence.

A spectral analysis of the photonic jets has previously been carried out by Itagi et al. [11] for cylinders. They concluded that the evanescent field only makes small contributions to photonic jets properties which are mainly due to a particular phase distribution. Chen et al. also affirmed that photonic jets do not involve evanescent fields [1], but this still needed to be closely examined for spherical problems invoking a complete three-dimensional analysis.

In this work, numerical parameters are presented in section 2. The three dimensional spectral expansion of the field described in section 3 permits a quantitative analysis of the contribution of the different spatial frequencies in photonic jets field distributions on section 4. The propagation of photonic jets is then studied in section 5 and comparised with Gaussian beams.

2. Simulations parameters

In the entire article, an incident wavelength in the optical range, $\lambda_v = 525\ nm$, is adopted so that the size parameter depends linearly on the sphere radius. At this wavelength, latex spheres have a refractive index of $N_s = 1.6$. The surrounding medium is considered to be either air, $N_0 = 1$, or water, $N_0 = 1.33$. The index contrast will then be respectively equal to $\rho = 1.6$, or $\rho = 1.2$.

The intensity distribution produced by a latex microsphere of radius 1 μm in water illuminated by a plane wave is simulated in Fig. 1*a*. The photonic jet can roughly be described with 4 parameters displayed in Fig. 1*b*: the 'focal' distance f from the surface of the sphere to the point of maximum intensity, the intensity enhancement I_{max}, at the 'focus', the beam waist w_0 at the focus and finally the 'diffraction length' z_r. These last two parameters will be precisely defined in the next section analogously to Gaussian beam parameters.

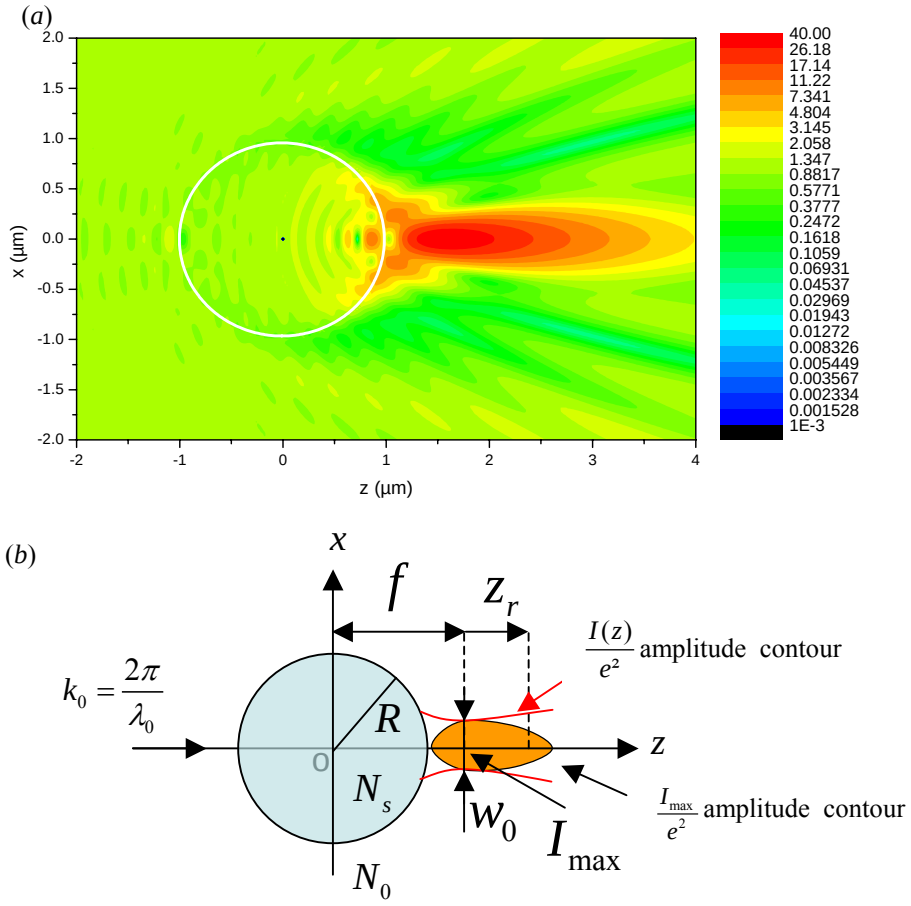

Fig. 1. Photonic jet produced when a dielectric sphere of radius $R = 1\ \mu m$, and refractive index N_s is illuminated by a plane wave propagating along the z axis in a homogeneous embedding medium of refractive index N_0 ($\rho = N_s/N_0 = 1.2$, $\lambda_v = 525\ nm$, $\lambda_0 = \lambda_v/N_0$). (*a*) a hot scale map of a photonic jet is displayed on a logarithmic scale of the electric field intensity. (*b*) A schema for photonic jet parameters is provided: 'focal' distance f , maximum enhancement I_{max} , width at the waist w_0 and diffraction length z_r . The amplitude contours of the photonic jet at $I(z)/e^2$ and I_{max}/e^2 are also displayed.

3. Spatial and spectral study of photonic jets

The numerical code permits the calculation of the total and scattered field of an incident field interacting with a microsphere throughout all space. To characterize photonic jets, the intensity enhancement of the EM field has been displayed on two axes of interest: the propagation axis z and a transverse axis x at $z = f$. An example is presented in Fig. 2, for $R = 1\ \mu m$ and $\rho = 1.2$. It has been found that the intensity enhancement along the propagation axis z, displayed in Fig. 2*a*, can be fitted in its decreasing part by a Lorentzian distribution. At the same time, the transversal intensity enhancement, displayed in Fig. 2*b* can predominantly be fitted by a Gaussian distribution. Therefore we define the diffraction length, z_r , as the half width of the photonic jet at the half maximum of the Lorentzian fit of the axial intensity

distribution, and the beam width, $w(z)$ as the transverse width at $I(z)/e^2$ of the Gaussian fitted distribution. The waist, w_0, of the photonic jet is then defined as the width at $z = f$.

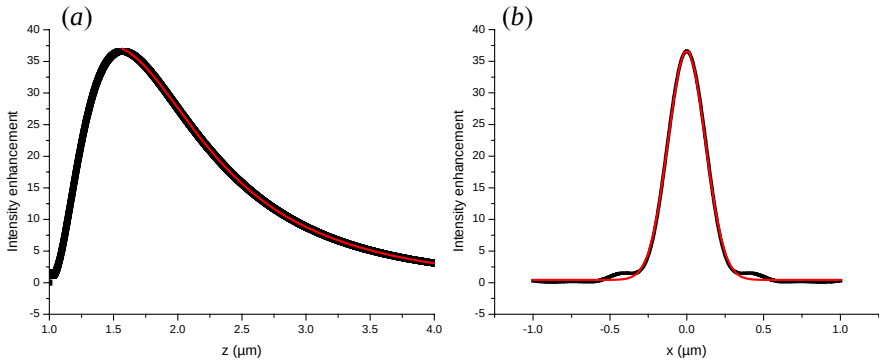

Fig. 2. Intensity enhancement distribution for a 1 μm radius sphere illuminated by a plane wave at λ_v = 525 nm with an index contrast of ρ = 1.2, $\lambda_0 = \lambda_v/N_0$ = 394 nm (*a*) along the propagation axis (*z*) (in black), and its Lorentzian fit (in red), z_r = 800 nm (*b*) along a transverse axis (*x*) for $z = f$ = 1.57 μm (in black), and its Gaussian fit (in red), w_0 = 241 nm =0.6λ_0.

Despite these similarities to Gaussian beam distributions, one expects photonic jets to differ from Gaussian beams, especially with respect to the way in which they propagate. The study of the spatial frequencies involved in the photonic jets field distribution will be particularly useful in distinguishing photonic jets from Gaussian beams. A rigourous spectral analysis of the scattered field is performed here by expanding the partial waves on a basis of cylindrical Bessel functions to calculate the EM field.

In Lorentz-Mie theory, the scattered field is expanded on a set of Vector Spherical Wave Functions (VSWFs), commonly denoted $\mathbf{M}_{n,m}$ and $\mathbf{N}_{n,m}$ [12,13]:

$$\mathbf{E}_{\text{scat}}(r,\theta,\phi) = E_0 \sum_{n=1}^{\infty} \sum_{m=-n}^{n} f_{n,m}^{(h)} \mathbf{M}_{n,m}(k_0 r,\theta,\phi) + f_{n,m}^{(e)} \mathbf{N}_{n,m}(k_0 r,\theta,\phi) \tag{1}$$

where $f_{n,m}$ are the Mie coefficients for scattered field and $k_0 = 2\pi N_0/\lambda_v$ is the propagation wave vector in the surrouding medium. The other notations are defined in Appendix A. Expressing the transverse wavevector $\vec{\mathbf{K}}$ as:

$$\vec{\mathbf{K}} = K\cos\phi_k \hat{\mathbf{x}} + K\sin\phi_k \hat{\mathbf{y}}, \tag{2}$$

one can write a spectral decomposition of the outgoing VSWFs in the form:

$$\begin{aligned} \mathbf{M}_{n,m}(k_0 r_{//},\phi,z) &= \int_{K=0}^{\infty}\int_{\phi=0}^{2\pi} \mathbf{X}_{n,m}(\theta_k,\phi_k) \frac{e^{i(\vec{K}.\vec{r}_{//}+k_z|z|)}}{k_z} K dK d\phi_k \\ \mathbf{N}_{n,m}(k_0 r_{//},\phi,z) &= \int_{K=0}^{\infty}\int_{\phi=0}^{2\pi} \mathbf{Z}_{n,m}(\theta_k,\phi_k) \frac{e^{i(\vec{K}.\vec{r}_{//}+k_z|z|)}}{k_z} K dK d\phi_k \end{aligned} \tag{3}$$

where ($r_{//}$, ϕ, z) are cylindrical coordinates and $k_z = \sqrt{k_0^2 - K^2}$. One can observe that the VSWFs can be interpreted as spatial Fourier transforms of the vector spherical harmonics. Spectral decompositions were here and henceforth restricted to the scattered field since they are unsuitable for describing incident plane waves (which have Dirac distributions at K=0).

To proceed further, we adopt the simplifying case of a sphere illuminated by a circularly right-polarized incident plane wave so that the field is entirely described by VSWFs with m = 1 (arbitrary polarization can of course be obtained by superpositions with circularly left polarized waves, m = -1). Using the Cartesian vector spherical harmonics, the scattered field can be written as:

$$\mathbf{E}_{\text{scat}}(r_{//},\phi,z) = E_0 \int_0^{\infty} \frac{K}{k_0} d\frac{K}{k_0} \begin{bmatrix} A(\frac{K}{k_0},\phi,z) J_0(Kr_{//}) \dfrac{\{\hat{\mathbf{x}} + i\hat{\mathbf{y}}\}}{\sqrt{2}} \\ B(\frac{K}{k_0},\phi,z) J_1(Kr_{//}) \hat{\mathbf{z}} \\ C(\frac{K}{k_0},\phi,z) J_2(Kr_{//}) \dfrac{\{\hat{\mathbf{x}} - i\hat{\mathbf{y}}\}}{\sqrt{2}} \end{bmatrix} \quad \text{with} \quad \begin{aligned} A &= \sum_{n=0}^{\infty} f_n^{(h)} A_n^{(h)} + f_n^{(e)} A_n^{(e)} \\ B &= \sum_{n=0}^{\infty} f_n^{(h)} B_n^{(h)} + f_n^{(e)} B_n^{(e)} \\ C &= \sum_{n=0}^{\infty} f_n^{(h)} C_n^{(h)} + f_n^{(e)} C_n^{(e)} \end{aligned} \quad (4)$$

where details and full expressions are relegated to Appendix B. This expansion provides a spectral representation of the field via three different coefficient functions, *A*, *B*, and *C*. The *B* and *C* coefficients correspond to depolarization contributions to the field and are generally quite weak when compared to those arising via the *A* coefficient, and we consequently focus attention henceforth on the *A* coefficient.

The amplitude of the *A* coefficient is presented in Fig. 3 as a function of the normalized radial spatial frequencies K/k_0 for a sphere of radius $R = 1\ \mu m$ at the position $\phi = 0$, $z = 1.05\ \mu m$. *A* is normalized to 1 at $K = 0$, and plotted for two different index contrasts $\rho = 1.2$ in Fig. 3*a* and $\rho = 1.6$ in Fig. 3*b*. The radial spectrum has the following features: a generally decreasing and oscillating features in the region $0 < K/k_0 < 1$ corresponding to propagative fields, a singularity originating from the homogeneous medium Green function at $K/k_0 = 1$ and a monotonically decreasing behaviour when $K > k_0$ for evanescent field contributions.

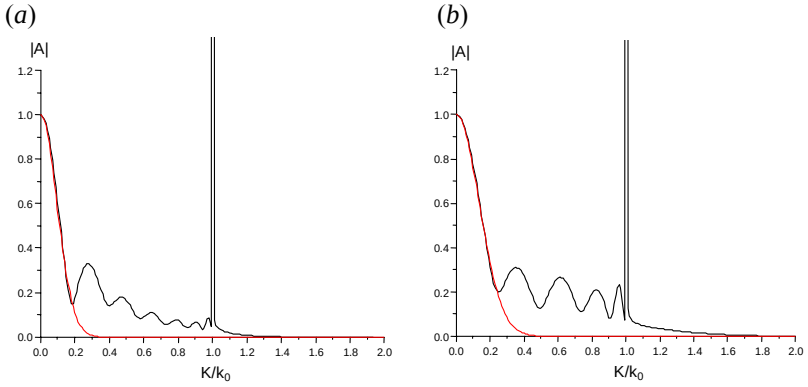

Fig. 3. Amplitude of the *A* coefficient as a function of normalized spatial frequencies K/k_0 at $z = 1.05\ \mu m$, for a sphere of radius $R = 1\mu m$, and index contrasts (*a*) $\rho = 1.2$ and (b) $\rho = 1.6$, illuminated by a plane wave at $\lambda_v = 525\ nm$. The low frequencies are respectively fitted by a Gaussian frequency distribution of respective widths $K/k_{0=}$=0,190 in (*a*) and $K/k_{0=}$=0,270 in (b) (red line).

The propagative frequency decomposition can be separated in two regions. From the zero-frequency to the first minimum, the spectral distribution is essentially described by a narrow Gaussian-type distribution which would give rise in direct space to a weakly focused Gaussian beam. In contrast, a highly focused Gaussian beam would have a large Gaussian spectral distribution. The secondary maxima and minima which can be observed in the higher spatial propagative frequencies enrich the jet spectrum. They allow photonic jets to have different features than Gaussian beam in direct space. By comparing Fig. 3*b* with Fig. 3*a*, one can see that higher index contrast enhances the high spatial frequency components which results in a stronger focalization and a narrower photonic jet.

One can also deduce from Fig. 3 that the strength of the evanescent field contribution depends significantly on the refraction index contrast and position at which the spectral decomposition is carried out. This dependence is highlighted in Fig. 4, which displays a hot scale map of the amplitude of the *A* coefficient as a function of the position along the

propagation axis z and the radial frequencies K/k_0 for refraction index contrasts $\rho = 1.2$ in (a) and $\rho = 1.6$ in (b). For both index contrasts, the evanescent field is considerably attenuated after distances of more than 500 *nm*. Consequently, for low index contrasts, like $\rho = 1.2$ where $f = 1.6$ μm, the evanescent field will not make any significant contributions to the narrow waist properties of the photonic jet. For $\rho = 1.6$, the photonic jet is on the surface of the sphere so that contribution of the evanescent field may be important. This point and the influence of the high propagative spatial frequencies will be discussed in the next section.

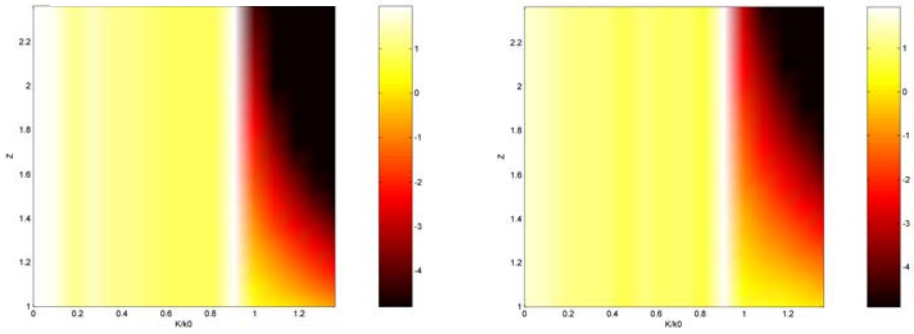

Fig. 4. Amplitude of the A coefficient as a function of z and K/k_0 in logarithmic scale with the same parameters as used in Fig. 3a and Fig. 3b respectively.

In this section we have presented a rigorous and analytical spectral expansion of three dimensional photonic jets. The next section will demonstrate how this tool can aid in analyzing the properties of photonic jets and bring new elements to the understanding of the unique features of photonic jets in direct space.

4. Photonic jet analysis

4.1 Direct space analysis of evanescent and propagative spectral contributions

Using the spectral expansion of Eq.(4), one can plot the spatial distribution after having explicitly filtered out all evanescent (i.e. $K > k_0$) contributions. The photonic jet scattered intensity along the propagation axis is plotted in red in figure Fig. 5a) while the intensity with the evanescent field removed is plotted in green. The same procedure is studied in Fig. 5b) for the transverse intensity at $z = f$. One remarks that when the evanescent field is removed, the maximum intensity position of the photonic jet moves away from the surface, the maximum field enhancement drops by half its value and the size of the waist is increased by 20 percent (from 214 *nm* to 256 *nm*). This example demonstrates that the evanescent field plays a significant role in the field distribution of photonic jets close to the surface of the sphere, which is the case when index contrasts are large. Nevertheless, the evanescent field cannot be held responsible for the principal photonic jet features, particularly when refractive index contrast is low.

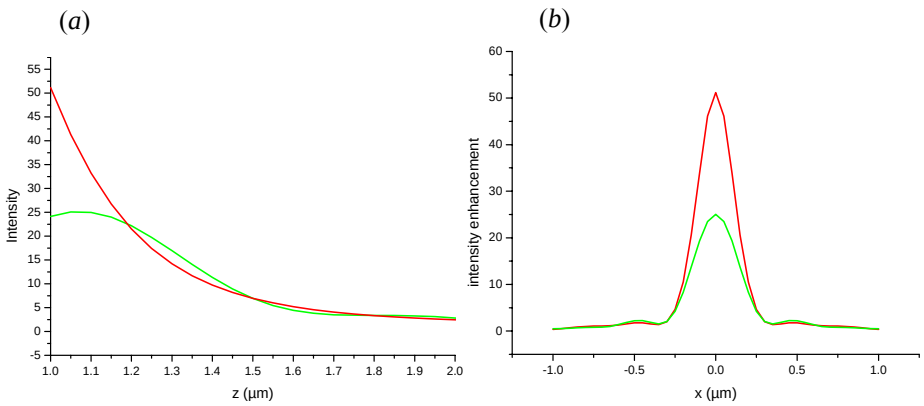

Fig. 5. Intensity distribution of the scattered intensity of the electric field: (*a*) along the propagation axis (z), and (*b*) at $z = f$, for sphere of radius $R = 1\mu m$ illuminated at $\lambda_v = 525\ nm$ for an index contrast of $\rho = 1.6$. The red curve corresponds to the full scattered intensity while the green curve is the intensity once the evanescent field has been removed.

The spectral expansion of the previous section showed a rich structure in the high spatial frequency components of the photonic jet. In direct space, each propagative spatial frequency corresponds to propagation at given angle with respect to the beam axis. An intensity map of a photonic jet is presented on a colored map in Fig. 6 (with $\rho = 1.6$). The angles corresponding respectively to the first few maxima and the minima of the amplitude of the *A* coefficient (cf. Fig. 3*b*) are displayed respectively with red lines and black lines in this figure. The maxima correspond to high intensity angles while the minima correspond to angles of low intensity regions. The maxima in the spectral distribution can therefore be associated with the presence of secondary lobes in the direct field structure. The first secondary lobes tend to confine the central lobe into a low divergent beam, while the secondary lobes with high transverse components tend to reduce the length and the waist of photonic jets.

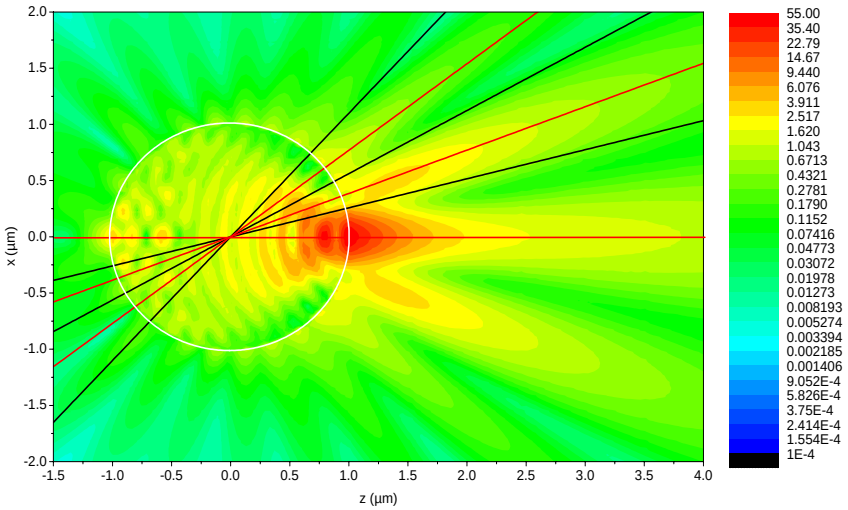

Fig. 6. Scattered intensity of a photonic jet produced by a sphere of radius 1 μm, illuminated at $\lambda_v = 525\ nm$ with an index contrast of $\rho = 1.6$. The angles corresponding to the maxima and minima in the spatial frequency expansion of Fig. 3*b* are displayed in direct space by red lines and black lines respectively.

The properties of the field scattered by microsphere illuminated by a plane wave has been studied without including the incident field. The incident field contributions to the principal

beam (i.e. photonic jet) are actually rather weak, except in the case of low index contrasts where they reduce the Rayleigh length. It will however be demonstrated in section 5 that the 'total' photonic jets still can have particularly low divergences when index contrasts are low. Therefore, the restriction to the study of the scattered field spectrum appears sufficient to highlight the distinctive physical properties of photonic jets.

4.2 Origin of the secondary lobes

The origin of secondary lobes illustrated in Fig. 6 can be found in the spherical geometry of the microspheres and the corresponding spherical geometry of VSWFs (or multipolar waves) which are eigenmodes of the spherical Maxwell propagation equation. The amplitude of the scattered field coefficients, $|f^{(h)}_{n,1}|$ and $|f^{(e)}_{n,1}|$ in this expansion are displayed in Fig. 7, where we recall that scattered field in the VSWF basis is expressed:

$$\mathbf{E}_{\text{scat}}(r,\theta,\phi) = E_0 \sum_{n=1}^{\infty} \sum_{m=-n}^{n} f^{(h)}_{n,m} \mathbf{M}_{n,m}(k_0 r,\theta,\phi) + f^{(e)}_{n,m} \mathbf{N}_{n,m}(k_0 r,\theta,\phi) \tag{5}$$

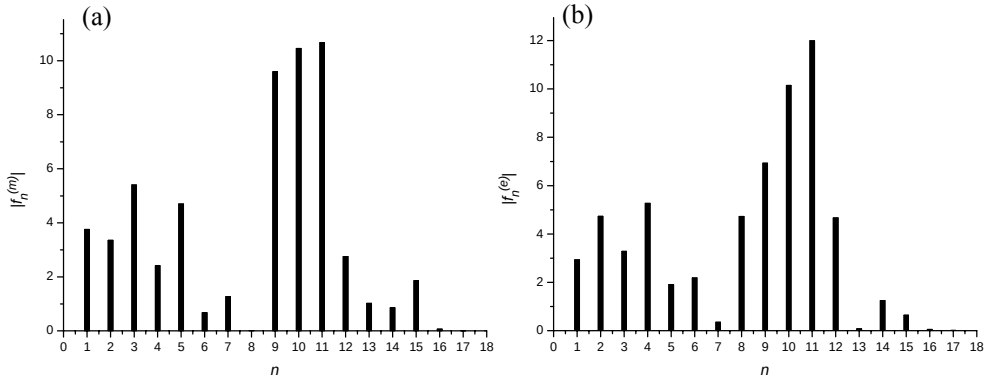

Fig. 7. Amplitude of scattered coefficients of photonic jets in the VSWF expansion; (a) for the magnetic $|f^{(h)}_{n,1}|$ coefficients, (b) for the electric $|f^{(e)}_{n,1}|$ coefficients. $R = 1\mu m$, $\rho = 1.6$, $\lambda_v = 525$ *nm*.

Fig. 7 illustrates that photonic jets can be seen as finite linear superpositions of high order VSWF, used to describe the EM field in the context of a rigorous EM theory. The scattered intensity of the term of VSWFs of order $n = 11$, which slightly dominates is displayed in Fig. 8. $|f^{(h)}_{11}\,\mathbf{M}_{11,1}|^2$ is displayed in Fig. 8*a* and $|f^{(e)}_{11}\,\mathbf{N}_{11,1}|^2$ in Fig. 8*b*. The VSWFs waves have intensity distributions comprised of number of 'beams' (there are in fact $2n$ 'beams' in a VSWF of order n). The secondary beams seen in Figs.1 and 6 are therefore intrinsically present in the VSWFs.

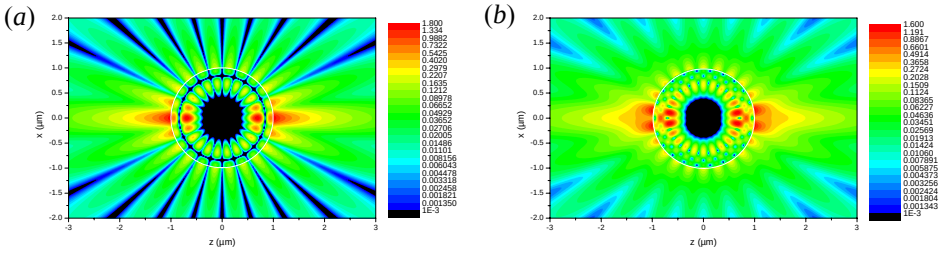

Fig. 8. Scattered intensity of the terms of order $n = 11$, (*a*) $|f^{(h)}_{11}\,\mathbf{M}_{11,1}|^2$, (*b*) $|f^{(e)}_{11}\,\mathbf{N}_{11,1}|^2$.

$R = 1\mu m$, $\rho = 1.6$, $\lambda_v = 525$ *nm*.

The superposition of the 3 principal orders of this photonic jet, $n = 9$, $n = 10$ and $n = 11$ (cf. Fig. 7) is displayed in Fig. 9.

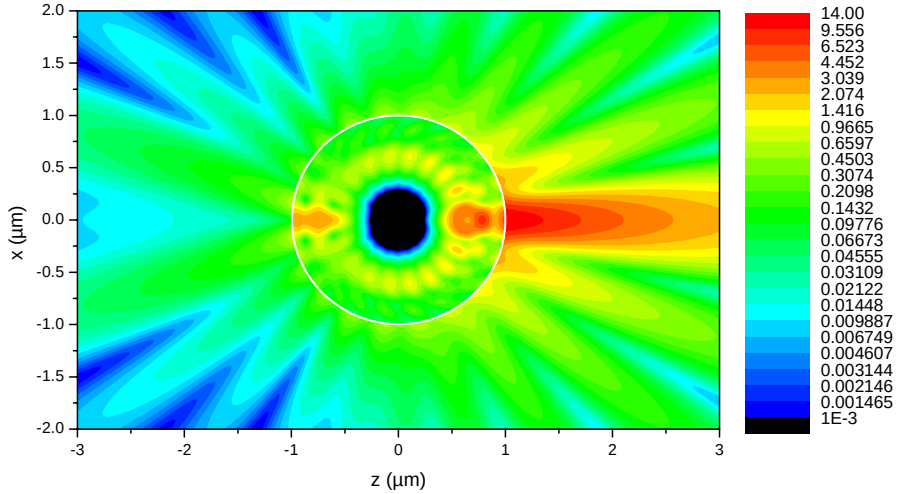

Fig. 9. Scattered intensity in $\log_{10}$ hot scale of a "photonic jet" generated with the 3 principal orders in the VSWF expansion: $n = 9$, $n = 10$ and $n = 11$, i.e. $\left|\sum_{n=9}^{11} f_n^{(h)}\mathbf{M}_{n,1} + f_n^{(e)}\mathbf{N}_{n,1}\right|^2$. $R = 1$ μm, $\rho = 1.6$, $\lambda_v = 525$ nm

One can see from Fig. 9 that the finite superposition of the multipolar waves of different orders and type (**M** and **N**) tend to enhance the principal (forward direction) beam and reduce the intensity of the secondary beams, especially in the backward direction. However, the forward secondary lobes still contain non negligible intensity.

In this section, the electromagnetic origin of the photonic jet has been demonstrated. The secondary beams emerge as a natural consequence of the geometry and the scale ($\lambda \sim R$) of the scatterers which requires an expansion on VSWFs. These secondary beams thus appear as the principal distinguishing feature of photonic jets with respect to the Gaussian beam behaviour generated in a paraxial optics approximation.

5. Photonic jet propagation

The study of photonic jet's spectrum in the previous sections has highligthed that high frequency lobes in the high spatial frequency spectra differ significantly from classic Gaussian beam spectra. These features have important visible repercussions in direct space and in particularly with regard to photonic jet propagation. Photonic jets have been said to diffract in a particularly low manner [1]. Let us compare the diffraction of 'total' photonic jets with Gaussian beams.

In the Gaussian beam model, the beam waist w_0 , and length z_r are linked by the relation $2z_r = k_0 w_0^2$ where k_0 is the wave number in the surrounding medium. One can inquire whether this relation continues to hold in the case of the photonic jet. To answer this question, we calculated for a given waist, the ratio between the associated Gaussian length and the numerically calculated jet length as a function of the sphere radius for $\rho = 1.2$ and $\rho = 1.6$. In the case $\rho = 1.2$, this ratio is close to 0.5 while for case $\rho = 1.6$, this ratio is closed to 1. This indicates that for high index contrasts, the decay length of photonic jet is similar to the Gaussian decay length but for low index contrasts, the decay length of the photonic jet is

twice greater than the Gaussian case. The Gaussian beams width at $1/e^2$ along the propagation axis z, is given by the relation:

$$w(z) = w_0\sqrt{1+\frac{(z-f)^2}{z_r^2}} \tag{6}$$

The computed width at $1/e^2$ (black curve) of the photonic jet is given in Fig. 10 as a function of z. The width at $1/e^2$ obtained from Eq.(6) for a Gaussian beam with identical waist and Rayleigh length is displayed in red in Fig. 10. Even if an agreement exists near the waist along a Rayleigh length (here $z_r \approx 1\ \mu m$), the relation of Eq.(6) does not enable a detailed prediction of the width of photonic jets. The divergence of the photonic jet is visibly lower than for a Gaussian beam with the same parameters w_0 and z_r (Fig. 10).

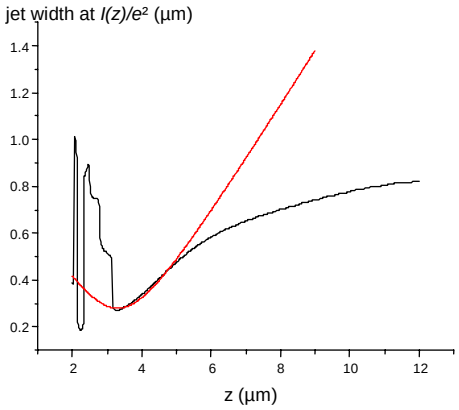

Fig. 10. Width of the photonic jet at $I(z)/e^2$ (black) and the associated Gaussian beam width (red curve) for a 2 μm radius sphere illuminated by a plane wave at λ_v = 525 nm for an index contrast of ρ = 1.2

For low index contrasts, a microsphere can easily create a highly collimated beam with a waist and a divergence at least twice smaller than a Gaussian beam created by current high numerical aperture optical lenses. This confirms what was observed I, the reciprocal space in previous sections. The beam created by a microsphere illuminated by an optical plane wave has a richer spectrum than a classical Gaussian beam, leading to unique propagation features in direct space.

Conclusion

A three dimensional spectral analysis demonstrating the rich structure of photonic jets has been performed. This permits the study of the contributions from all spatial frequency components (both propagative and evanescent). This decomposition indicates predominantly propagative wave contributions whose low frequency components are essentially of a Gaussian type combined with high spatial frequency distributed components corresponding to secondary lobes in direct space, for an overall behaviour corresponding to highly focused beams. The evanescent field contributions to photonic jets created by microspheres have been demonstrated to play an important role, enhancing and sharpening the photonic jets field distribution, but not particularly involved in the low divergence properties photonic jets. It has been shown that the highly collimated low divergence properties of photonic jets observed with low index contrast spheres is principally due to the presence of the secondary beams

associated with the multipole nature of electromagnetic field interacting with micro-sphere. When the same sphere is embedded in air, the higher index contrast produces a more localized beam both in the radial and in the longitudinal directions. The fact that such simple and inexpensive optical components as dielectric micro-spheres provides beams can produce beams of such unique and potentially useful properties, opens up numerous perspectives for applications.

Acknowledgments

The authors acknowledge stimulating discussions with Jérome Wenger, Ross McPhedran, Gérard Tayed and Phillipe Delaporte. This work has been funded by the grant PEPS "NANODRILL" of the Centre National de la Recherche Scientifique.

Appendix A : Numerical simulations

Home developed numerical codes based on Mie theory are used to perform the study. In this context, the electromagnetic field is expanded on the vector partial waves (also called the Vector Spherical Wave Functions VSWFs), commonly denoted $\mathbf{M}_{n,m}$ and $\mathbf{N}_{n,m}$ [12] :

$$\begin{aligned}\mathbf{M}_{n,m}\left(k_0 r,\theta,\phi\right) &= h_n^{(+)}\left(k_0 r\right)\mathbf{X}_{n,m}\left(\theta,\phi\right)\\ \mathbf{N}_{n,m}\left(k_0 r,\theta,\phi\right) &= \frac{1}{k_0 r}\left[h_n^{(+)}\left(k_0 r\right)\mathbf{Y}_{n,m}\left(\theta,\phi\right)+\left(k_0 r\, h_n^{(+)}\left(k_0 r\right)\right)'\mathbf{Z}_{n,m}\left(\theta,\phi\right)\right]\end{aligned} \tag{7}$$

where $k_0 = 2\pi N_0/\lambda_v$ where λ_v is the incident vacuum wavelength and N_0 is the refractive index of the surrounding medium. The **Y, Z,** and **X** in eq.(1) are vector spherical harmonics (VSHs) defined in spherical coordinates by [13] as:

$$\begin{aligned}\mathbf{Y}_{n,m}\left(\theta,\phi\right) &\equiv \hat{\mathbf{r}}Y_{n,m}\left(\theta,\phi\right)\\ \mathbf{Z}_{n,m}\left(\theta,\phi\right) &\equiv \frac{r\nabla\mathbf{Y}_{n,m}\left(\theta,\phi\right)}{\sqrt{n\left(n+1\right)}}\\ \mathbf{X}_{n,m}\left(\theta,\phi\right) &\equiv \mathbf{Z}_{n,m}\left(\theta,\phi\right)\times\hat{\mathbf{r}}\end{aligned} \tag{8}$$

Singularity free partial waves are obtained by taking the regular part, denoted *Rg*, wherein the outgoing spherical Hankel functions h_n are replaced by spherical Bessel functions, j_n:

$$\begin{aligned}Rg\left\{\mathbf{M}_{n,m}\left(k_0 r,\theta,\phi\right)\right\} &= j_n\left(k_0 r\right)\mathbf{X}_{n,m}\left(\theta,\phi\right)\\ Rg\left\{\mathbf{N}_{n,m}\left(k_0 r,\theta,\phi\right)\right\} &= \frac{1}{k_0 r}\left[j_n\left(k_0 r\right)\mathbf{Y}_{n,m}\left(\theta,\phi\right)+\left(k_0 r\, j_n\left(k_0 r\right)\right)'\mathbf{Z}_{n,m}\left(\theta,\phi\right)\right]\end{aligned} \tag{9}$$

These regular partial wave vectors are used to expand the incident and the internal field:

$$\begin{aligned}\mathbf{E}_{\text{inc}}(r,\theta,\phi) &= E_0\sum_{n=1}^{\infty}\sum_{m=-n}^{n} a_{n,m}^{(h)}Rg\left\{\mathbf{M}_{n,m}(k_s r,\theta,\phi)\right\}+a_{n,m}^{(e)}Rg\left\{\mathbf{N}_{n,m}(k_s r,\theta,\phi)\right\}\\ \mathbf{E}_{\text{int}}(r,\theta,\phi) &= E_0\sum_{n=1}^{\infty}\sum_{m=-n}^{n} s_{n,m}^{(h)}Rg\left\{\mathbf{M}_{n,m}(k_s r,\theta,\phi)\right\}+s_{n,m}^{(e)}Rg\left\{\mathbf{N}_{n,m}(k_s r,\theta,\phi)\right\}\end{aligned} \tag{10}$$

where $k_s = 2\pi N_s/\lambda_v = \rho k_0$ and N_s the refractive index of the sphere with $\rho = N_s/N_0 = k_s/k_0$ the refractive index contrast.The a_{nm} and s_{nm} are respectively the incident and internal coefficients in the field expansion. E_0 is a real parameter determining the incident field amplitude. For plane waves, these coefficients are:

$$\begin{aligned} a_{n,m}^{(h)} &= 4\pi i^n \mathbf{X}_{n,m}^*(\theta,\phi).\hat{\mathbf{e}}_i \\ a_{n,m}^{(e)} &= 4\pi i^{n-1} \mathbf{Z}_{n,m}^*(\theta,\phi).\hat{\mathbf{e}}_i \end{aligned} \tag{11}$$

where $\hat{\mathbf{e}}_i$ is the incident field polarization. The EM wave is circularly polarized to facilitate the analysis:

$$\hat{\mathbf{e}}_i = \frac{\hat{\mathbf{x}} + i\hat{\mathbf{y}}}{\sqrt{2}} \tag{12}$$

This choice renders the intensity axi-symmetric so that intensity maps in different planes are equivalent. The scattered field is expanded on the partial wave vectors:

$$\mathbf{E}_{\text{scat}}(r,\theta,\phi) = E_0 \sum_{n=1}^{\infty} \sum_{m=-n}^{n} f_{n,m}^{(h)} \mathbf{M}_{n,m}(k_0 r,\theta,\phi) + f_{n,m}^{(e)} \mathbf{N}_{n,m}(k_0 r,\theta,\phi) \tag{13}$$

where $f_{n,m}$ are the scattered coefficients in the field expansion. The boundary conditions at the surface of the sphere, $r = R$, enable one to link the scattered field coefficients with the incident field coefficients via the 'Mie' coefficients:

$$\begin{aligned} f_{n,m}^{(h)} &= \frac{\psi_n'(k_0 R)\psi_n(k_s R) - \rho\psi_n'(k_s R)\psi_n(k_0 R)}{\rho\xi_n'(k_0 R)\psi_n(k_s R) - \psi_n'(k_s R)\xi_n(k_0 R)} a_{n,m}^{(h)} \\ f_{n,m}^{(e)} &= \frac{\psi_n'(k_s R)\psi_n(k_0 R) - \rho\psi_n'(k_0 R)\psi_n(k_s R)}{\rho\xi_n'(k_0 R)\psi_n(k_s R) - \psi_n'(k_s R)\xi_n(k_0 R)} a_{n,m}^{(e)} \end{aligned} \tag{14}$$

where $\psi_n(x) \equiv x j_n(x)$ and $\xi_n(x) \equiv x h_n^{(+)}(x)$ are the Ricatti Bessel functions. The 'Mie' coefficients only depend on the size parameter $k_0 R$ and the refractive index contrast between the two media, ρ. It is usually sufficient to adopt the Wiscombe criterion for the truncation of convergence of numerical simulations as a limit for the truncation of the basis [14].

Appendix B: Spectral expansion of the electromagnetic field

The spectral expansion of the EM field distribution of photonic jets is can be obtained via an integral expansion of the VSWFs on a cylindrical coordinates and invoking Clebsch Gordan coefficients. In the Lorentz-Mie theory, the scattered EM field is expanded on the basis of VSWFs:

$$\mathbf{E}_{\text{scat}}(r,\theta,\phi) = E_0 \sum_{n=1}^{\infty} \sum_{m=-n}^{n} f_{n,m}^{(h)} \mathbf{M}_{n,m}(k_0 r,\theta,\phi) + f_{n,m}^{(e)} \mathbf{N}_{n,m}(k_0 r,\theta,\phi) \tag{15}$$

where

$$\begin{aligned} \mathbf{M}_{n,m}(k_0 r,\theta,\phi) &= h_n^{(+)}(k_0 r)\mathbf{X}_{n,m}(\theta,\phi) \\ \mathbf{N}_{n,m}(k_0 r,\theta,\phi) &= \frac{1}{k_0 r}\left[h_n^{(+)}(k_0 r)\mathbf{Y}_{n,m}(\theta,\phi) + \left(k_0 r h_n^{(+)}(k_0 r)\right)' \mathbf{Z}_{n,m}(\theta,\phi) \right] \end{aligned} \tag{16}$$

and $\mathbf{X}_{n,m}$, $\mathbf{Y}_{n,m}$ and $\mathbf{Z}_{n,m}$ are the vector spherical harmonics and h_n is the spherical outgoing Hankel function. E_0 is a real parameter determining the incident field amplitude. It can be shown in the scalar case that:

$$h_n(k_0 r) Y_{n,m}(\hat{r}) = \frac{1}{2\pi i^n k_0} \int_{K=0}^{\infty} \int_{\phi_k=0}^{2\pi} K dK d\phi_k Y_{n,m}(\hat{k}) \frac{e^{\pm i\vec{k}.\vec{r}}}{k_z} \qquad \text{sign}(z) = \pm \tag{17}$$

where $k_z = \sqrt{k_0^2 - K^2}$. $Y_{n,m}$ are the scalar spherical harmonics set as :

$$Y_{n,m}(\theta,\phi) = c_{n,m} P_n^m(\cos\theta) e^{im\phi} \tag{18}$$

where P_n^m are the associated Legendre polynomials and $c_{n,m}$ is a normalization factor:

$$c_{n,m} = \left[\frac{2n+1}{4\pi} \frac{(n-m)!}{(n+m)!} \right]^{1/2} \tag{19}$$

Using the spherical unit vectors:

$$\hat{\boldsymbol{\chi}}_{-1} = \frac{\hat{\mathbf{x}} - i\hat{\mathbf{y}}}{\sqrt{2}}, \quad \hat{\boldsymbol{\chi}}_0 = \hat{\mathbf{z}}, \quad \hat{\boldsymbol{\chi}}_1 = -\frac{\hat{\mathbf{x}} + i\hat{\mathbf{y}}}{\sqrt{2}} \tag{20}$$

where $\hat{x}, \hat{y}, \hat{z}$ are the cartesian unit vectors, and using the Cartesian vector spherical harmonics defined by:

$$\mathbf{Y}_{n,l}^m = \sum_{\mu=-1}^{1} (l, m-\mu; 1, \mu \mid n, m) Y_{l,m-\mu} \hat{\boldsymbol{\chi}}_\mu \tag{21}$$

where $(l, m-\mu; 1, \mu \mid n, m)$ are the Clebsch-Gordan coefficients, the vectorial spherical harmonics can be written in terms of cartesian spherical harmonics as:

$$\begin{aligned} \mathbf{X}_{n,m} &= \frac{\mathbf{Y}_{n,n}^m}{i} \\ \mathbf{Y}_{n,m} &= \sqrt{\frac{n}{2n+1}} \mathbf{Y}_{n,n-1}^m + \sqrt{\frac{n+1}{2n+1}} \mathbf{Y}_{n,n+1}^m \\ \mathbf{Z}_{n,m} &= \sqrt{\frac{n+1}{2n+1}} \mathbf{Y}_{n,n-1}^m - \sqrt{\frac{n}{2n+1}} \mathbf{Y}_{n,n+1}^m \end{aligned} \tag{22}$$

The vector function analogue of eq.(15) is :

$$\begin{aligned} \mathbf{M}_{n,m}(k_0 r_{//}, \phi, z) &= \int_{K=0}^{\infty} \int_{\phi=0}^{2\pi} \mathbf{X}_{n,m}(\theta_k, \phi_k) \frac{e^{i(\vec{K}.\vec{r}_{//} + k_z |z|)}}{k_z} K dK d\phi_k \\ \mathbf{N}_{n,m}(k_0 r_{//}, \phi, z) &= \int_{K=0}^{\infty} \int_{\phi=0}^{2\pi} \mathbf{Z}_{n,m}(\theta_k, \phi_k) \frac{e^{i(\vec{K}.\vec{r}_{//} + k_z |z|)}}{k_z} K dK d\phi_k \end{aligned} \tag{23}$$

The exponential part can be expanded as :

$$e^{i\mathbf{K}.\mathbf{r}_{//}} = e^{iKr_{//}\cos(\phi_k - \phi)} \tag{24}$$

The integral according to ϕ_k can be analytically calculated using [15]

$$\int_0^{2\pi} e^{ix\cos(\phi_k - \phi)} e^{in\phi_k} d\phi_k = 2\pi i^n J_n(x) e^{in\phi} \tag{25}$$

Where J_n are the cylindrical Bessel functions

Proceeding further, we obtain:

$$\mathbf{E}_{\text{scat}}(r_{//}, \phi, z) = E_0 \sum_{n=1}^{\infty} \int_0^{\infty} \frac{K}{k_0} d \frac{K}{k_0} f_n^{(h)} \begin{bmatrix} A_n^{(h)}(\frac{K}{k_0}, \phi, z) J_0(Kr_{//}) \dfrac{\{\hat{\mathbf{x}} + i\hat{\mathbf{y}}\}}{\sqrt{2}} \\ B_n^{(h)}(\frac{K}{k_0}, \phi, z) J_1(Kr_{//}) \hat{\mathbf{z}} \\ C_n^{(h)}(\frac{K}{k_0}, \phi, z) J_2(Kr_{//}) \dfrac{\{\hat{\mathbf{x}} - i\hat{\mathbf{y}}\}}{\sqrt{2}} \end{bmatrix} + f_n^{(e)} \begin{bmatrix} A_n^{(e)}(\frac{K}{k_0}, \phi, z) J_0(Kr_{//}) \dfrac{\{\hat{\mathbf{x}} + i\hat{\mathbf{y}}\}}{\sqrt{2}} \\ B_n^{(e)}(\frac{K}{k_0}, \phi, z) J_1(Kr_{//}) \hat{\mathbf{z}} \\ C_n^{(e)}(\frac{K}{k_0}, \phi, z) J_2(Kr_{//}) \dfrac{\{\hat{\mathbf{x}} - i\hat{\mathbf{y}}\}}{\sqrt{2}} \end{bmatrix} \tag{26}$$

Where we assume that the plane wave is circularly right polarized so that only $\mathbf{M}_{n,1}(k_0 r_{//},\phi,z)$ and $\mathbf{N}_{n,1}(k_0 r_{//},\phi,z)$ contribute to the field expansion and

$$A_n^{(h)} = \frac{-1}{i^{n+1}}(n,0;1,1\,|\,n,1)c_{n,0}P_n^0\left(\sqrt{1-\frac{K}{k_0}}\right)\frac{e^{ik_0|z|\sqrt{1-\frac{K}{k_0}}}}{\sqrt{1-\frac{K}{k_0}}}$$

$$B_n^{(h)} = \frac{1}{i^{n}}(n,1;1,0\,|\,n,1)c_{n,1}P_n^1\left(\sqrt{1-\frac{K}{k_0}}\right)e^{i\phi}\frac{e^{ik_0|z|\sqrt{1-\frac{K}{k_0}}}}{\sqrt{1-\frac{K}{k_0}}} \tag{27}$$

$$C_n^{(h)} = \frac{-1}{i^{n+1}}(n,2;1,-1\,|\,n,1)c_{n,2}P_n^2\left(\sqrt{1-\frac{K}{k_0}}\right)e^{2i\phi}\frac{e^{ik_0|z|\sqrt{1-\frac{K}{k_0}}}}{\sqrt{1-\frac{K}{k_0}}}$$

and

$$A_n^{(e)} = \frac{-1}{i^{n-1}}\left[\begin{array}{l}\sqrt{\frac{n+1}{2n+1}}(n-1,0;1,1\,|\,n,1)c_{n-1,0}P_{n-1}^0\left(\sqrt{1-\frac{K}{k_0}}\right)\\ +\sqrt{\frac{n}{2n+1}}(n+1,0;1,1\,|\,n,1)c_{n+1,0}P_{n+1}^0\left(\sqrt{1-\frac{K}{k_0}}\right)\end{array}\right]\frac{e^{ik_0|z|\sqrt{1-\frac{K}{k_0}}}}{\sqrt{1-\frac{K}{k_0}}}$$

$$B_n^{(e)} = \frac{i}{i^{n-1}}\left[\begin{array}{l}\sqrt{\frac{n+1}{2n+1}}(n-1,1;1,0\,|\,n,1)c_{n-1,1}P_{n-1}^1\left(\sqrt{1-\frac{K}{k_0}}\right)\\ +\sqrt{\frac{n}{2n+1}}(n+1,1;1,0\,|\,n,1)c_{n+1,1}P_{n+1}^1\left(\sqrt{1-\frac{K}{k_0}}\right)\end{array}\right]e^{i\phi}\frac{e^{ik_0|z|\sqrt{1-\frac{K}{k_0}}}}{\sqrt{1-\frac{K}{k_0}}} \tag{28}$$

$$C_n^{(e)} = \frac{-1}{i^{n-1}}\left[\begin{array}{l}\sqrt{\frac{n+1}{2n+1}}(n-1,2;1,-1\,|\,n,1)c_{n-1,2}P_{n-1}^2\left(\sqrt{1-\frac{K}{k_0}}\right)\\ +\sqrt{\frac{n}{2n+1}}(n+1,2;1,-1\,|\,n,1)c_{n+1,2}P_{n+1}^2\left(\sqrt{1-\frac{K}{k_0}}\right)\end{array}\right]e^{2i\phi}\frac{e^{ik_0|z|\sqrt{1-\frac{K}{k_0}}}}{\sqrt{1-\frac{K}{k_0}}}$$

In this notation, the scattered field is finally expressed:

$$\mathbf{E}_{\text{scat}}(r_{//},\phi,z) = E_0\int_0^\infty \frac{K}{k_0}d\frac{K}{k_0}\left[\begin{array}{l}A(\frac{K}{k_0},\phi,z)J_0(Kr_{//})\frac{\{\hat{\mathbf{x}}+i\hat{\mathbf{y}}\}}{\sqrt{2}}\\ B(\frac{K}{k_0},\phi,z)J_1(Kr_{//})\hat{\mathbf{z}}\\ C(\frac{K}{k_0},\phi,z)J_2(Kr_{//})\frac{\{\hat{\mathbf{x}}-i\hat{\mathbf{y}}\}}{\sqrt{2}}\end{array}\right] \text{ with } \begin{array}{l}A=\sum_{n=0}^{\infty} f_n^{(h)}A_n^{(h)} + f_n^{(e)}A_n^{(e)}\\ B=\sum_{n=0}^{\infty} f_n^{(h)}B_n^{(h)} + f_n^{(e)}B_n^{(e)}\\ C=\sum_{n=0}^{\infty} f_n^{(h)}C_n^{(h)} + f_n^{(e)}C_n^{(e)}\end{array} \tag{29}$$